electronics

MDPI

Article

A 28 GHz Broadband Helical Inspired End-Fire Antenna and Its MIMO Configuration for 5G Pattern Diversity Applications

Hijab Zahra [1,*], Wahaj Abbas Awan [2], Wael Abd Ellatif Ali [3], Niamat Hussain [4,*], Syed Muzahir Abbas [1,5] and Subhas Mukhopadhyay [1]

1 School of Engineering, Faculty of Science and Engineering, Macquarie University, Sydney, NSW 2109, Australia; syed.abbas@mq.edu.au (S.M.A.); subhas.mukhopadhyay@mq.edu.au (S.M.)
2 Department of Integrated IT Engineering, Seoul National University of Science and Technology, Seoul 01811, Korea; wahajabbasawan@seoultech.ac.kr
3 Department of Electronics & Communications Engineering, College of Engineering and Technology, Arab Academy for Science, Technology and Maritime Transport (AASTMT), Alexandria 1029, Egypt; wael.ali@aast.edu
4 Department of Computer and Communication Engineering, Chungbuk National University, Cheongju, Chungbuk 28644, Korea
5 BENELEC, Botany, Sydney, NSW 2019, Australia
* Correspondence: hijab.zahra@students.mq.edu.au (H.Z.); hussain512@ieee.org (N.H.)

Abstract: In this paper, an end-fire antenna for 28 GHz broadband communications is proposed with its multiple-input-multiple-output (MIMO) configuration for pattern diversity applications in 5G communication systems and the Internet of Things (IoT). The antenna comprises a simple geometrical structure inspired by a conventional planar helical antenna without utilizing any vias. The presented antenna is printed on both sides of a very thin high-frequency substrate (Rogers RO4003, $\varepsilon_r = 3.38$) with a thickness of 0.203 mm. Moreover, its MIMO configuration is characterized by reasonable gain, high isolation, good envelope correlation coefficient, broad bandwidth, and high diversity gain. To verify the performance of the proposed antenna, it was fabricated and verified by experimental measurements. Notably, the antenna offers a wide −10 dB measured impedance ranging from 26.25 GHz to 30.14 GHz, covering the frequency band allocated for 5G communication systems with a measured peak gain of 5.83 dB. Furthermore, a performance comparison with the state-of-the-art mm-wave end-fire antennas in terms of operational bandwidth, electrical size, and various MIMO performance parameters shows the worth of the proposed work.

Keywords: 28 GHz; end-fire antenna; millimeter-wave communication; IoT; Internet of things; 5G antenna

Citation: Zahra, H.; Awan, W.A.; Ali, W.A.E.; Hussain, N.; Abbas, S.M.; Mukhopadhyay, S. A 28 GHz Broadband Helical Inspired End-Fire Antenna and Its MIMO Configuration for 5G Pattern Diversity Applications. *Electronics* **2021**, *10*, 405. https://doi.org/10.3390/electronics10040405

Academic Editors: Reza K. Amineh and Paolo Baccarelli
Received: 9 December 2020
Accepted: 3 February 2021
Published: 7 February 2021

1. Introduction

The fifth-generation (5G) of mobile communications is expected to revolutionize the manner in which communications take place globally. This is based on a user-centric approach which will guarantee improved mobile broadband, and aims for a peak data rate of 20 Gbps [1]. Moreover, 5G technology is expected to upgrade the Internet of Things (IoT) capabilities of the current mobile network, which will be a transformation for future communication technologies [2]. Consequently, to achieve these highly promising features of 5G technology, antennas operating at the designated bands capable of supporting 5G functionalities are required [3]. In addition, 5G antennas must support other features, such as accurate beam coverage, and have the ability to meet the requirements of ever-changing scenarios [4]. In addition to reducing antenna losses to provide coverage with considerable depth and width, precise control of the antenna pattern to direct the beam towards the intended direction, and high spectral efficiency to allow the sharing of resources in the time and frequency domain between several users, are highly desired [5].

The technology of the 5G frequency spectrum depends on three frequency bands (sub-1 GHz, sub-6 GHz, and millimeter waves), the most important frequency band of which is 28 GHz (n257) [6]. The 28 GHz band is considered to be the most tested band in the world, mainly due to the availability of large portions of the unutilized spectrum around it, and due to the global availability of this band [7]. Furthermore, this frequency is preferable for the reduced complexity of the devices because of the better propagation compared to other millimeter frequencies [8]. A considerable amount of research has been devoted to the design of antennas operating at 28 GHz using different optimization techniques [9–14]. One of the commonly used types is the microstrip antenna, due to its advantage of design simplicity and its compactness, as demonstrated in [9,10]. Metasurface-based antennas have the advantages of wide bandwidth and high gain at the expense of bigger dimensions and profiles [11,12]. Antennas with defected ground structures (DGS) offer the advantages of wider operational bandwidth and compact size, but the disadvantage of complex geometrical structures [13–16]. Moreover, arrays of antennas provide high gain and wide bandwidth, however, the structures are complex with bigger dimensions [17,18]. Several designs have been reported for 5G mm-wave applications [19–21], in which the single element gain is in the range of 2dB to 6 dB.

In addition to other antenna types, end-fire antennas are also well-known due to their numerous advantages, including compact size, wideband, and high gain for radar and sensing applications. Although a large number of studies have used microwave frequency bands to obtain compact antennas with end-fire radiation patterns, few studies have been conducted using the mm-wave band spectrum. A dual-polarized end-fire antenna with an operational bandwidth of 3.03% was presented in [22], however, the antenna has a complex geometrical structure due to the presence of multiple vias and mesh grid structure. In [23], a broadband Yagi-Uda antenna is presented with a high gain of around 12 dB, but the antenna has a large dimension i.e., $5.6\lambda_C \times 1.6\lambda_C$. In [24,25], an SIW-fed antenna and planar helical antennas were proposed for V-band applications, respectively. Both presented works offer wide operational bandwidth of 11.67% and 25.5%, and high gain of 12 dB and 6.3 dB, respectively. However, these designs have a larger electrical size in conjunction with the presence of several vias that cause the structural complexity for mass production. Another interesting work was presented in [26], where a Yagi-Uda antenna with director and reflectors was designed to achieve a high gain of 7.82 dB and an impedance bandwidth of 12.5%. The antenna has a large overall size of $4.05\lambda_C \times 1.89\lambda_C$. Planar helical antennas have also been reported in [27,28], however, they also have complex designs with connecting via-holes.

After an in-depth study of the state-of-the-art antennas, it can be concluded that the design of a compact size antenna with a low level of complexity and characterized by good mechanical robustness, which can be implemented on the same printed circuit board as other electronic devices, is needed for upcoming 5G communication systems.

In this paper, an end-fire antenna is proposed for 28 GHz applications. The antenna is inspired by a planar helical shape for enhanced compactness to make it suitable for surface-mounted applications in 5G smart devices and IoT applications. The suggested antenna is characterized by a via-free simple geometrical structure, which significantly reduces the level of complexity combined with the advantages of wider bandwidth and higher gain. To fulfill the requirements of the multiple-input-multiple-output (MIMO) system, a single element was further utilized to design a two-element MIMO antenna characterized by a low envelope correlation coefficient (ECC), channel capacity loss (CCL), high mean effective gain (MEG), pattern diversity capability, and high efficiency. The remainder of the paper is organized as follows: antenna design is discussed in Section 2, simulation and measurement results are discussed in Section 3 and, finally, a conclusion is presented in Section 4.

2. Antenna Geometry and Design Methodology

This section presents the details for the proposed design geometry, and the design evolution and impact of design parameters.

2.1. Antenna Geometry

The geometrical configuration of the proposed end-fire antenna is shown in Figure 1. The antenna has a compact size, with a length (A_X) and width (A_Y), which correspond to $1.36\lambda_C \times 0.9\lambda_C$, where λ_C is the free-space wavelength at the central frequency of 28 GHz. The presented antenna is imprinted on both sides of Rogers RO4003 substrate with a thickness (H) of only 0.203 mm, dielectric constant (ε_r) of 3.38, and dissipation factor (tan δ) of 0.0027 [29]. The antenna was fed using a grounded coplanar waveguide (GCPW) technique. The radiator consists of a planar helical antenna with an inspired V-shaped structure, where both arms are expanded by an angle of θ. The backside of the substrate consists of a partial ground plane with a length L_3. A hole with a radius of 1 mm was etched from the substrate to insert the screw of the end-launch connector, which is used to feed the proposed antenna, as depicted in Figure 1d.

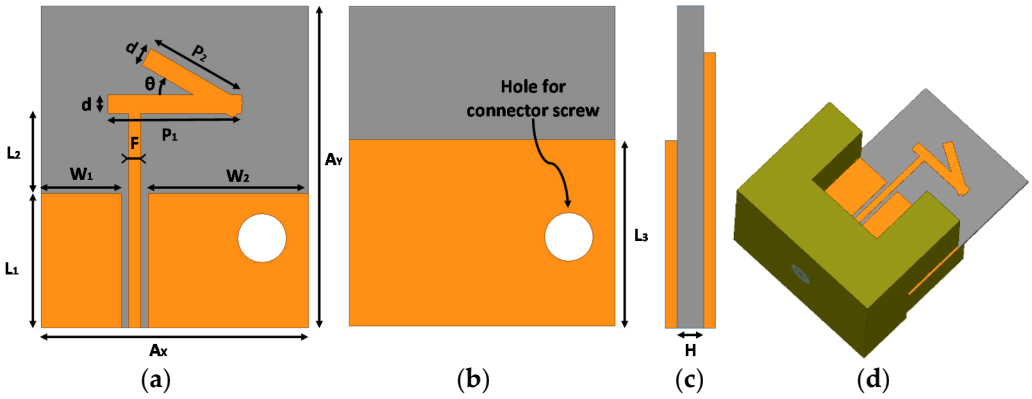

Figure 1. Geometry of proposed antenna (**a**) top view, (**b**) bottom view, (**c**) side view, and (**d**) 3-D model with end-launch connector.

2.2. Antenna Designing and Radiation Mechanism

The design methodology and various steps involved in the design of the proposed antenna are depicted in Figure 2. The antenna design comprises of the following three steps.

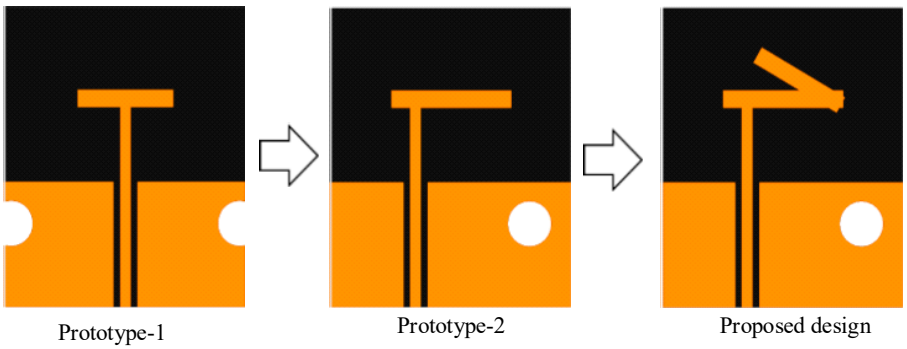

Figure 2. Design evolution of the proposed planar helix antenna.

Step-1: Design of a T-shaped monopole antenna operating at 28 GHz.

Step-2: Modifying the conventional T-shaped antenna to improve impedance bandwidth and end-fire radiation.

Step-3: Design of helical inspired broadband antenna to cover 28 GHz band spectrum with an end-fire radiation pattern.

First, a T-shaped GCPW fed monopole antenna was designed to resonate at the desired frequency (f_c) of 28 GHz. The length (P_1) of the monopole antenna was determined by using the following equation [30]:

$$P_1 = \frac{c}{4\, f_c\, \sqrt{\varepsilon_{eff}}} \tag{1}$$

where c is the free-space speed of light which is approximately equal to 3×10^8 m s^{-1}, and ε_{eff} is the effective dielectric constant of the substrate, which can be estimated by using the following relation [30]:

$$\varepsilon_{eff} \approx \frac{\varepsilon_r + 1}{2} + \frac{\varepsilon_r + 1}{2}\left(1 + 12\left(\frac{d}{h}\right)\right)^{-0.5} \tag{2}$$

where ε_r is the dielectric constant of the substrate, d is the width of the monopole, and h is the substrate thickness. The bandwidth of the T-shaped antenna was 650 MHz, ranging from 27.78 GHz to 28.43 GHz, as shown in Figure 3. The antenna exhibits a bi-directional radiation pattern due to equal distribution of current on both sides of the head of the T-shaped antenna, as depicted in Figure 4, with a maximum gain value of 3.96 dB, as illustrated in Figure 5. The bandwidth of the T-shaped antenna was not enough to cover the globally allocated band spectrum of 28 GHz with a range of 26.5–29.5 GHz. Moreover, the reported gain and radiation patterns were not suitable for 5G mm-wave communication systems.

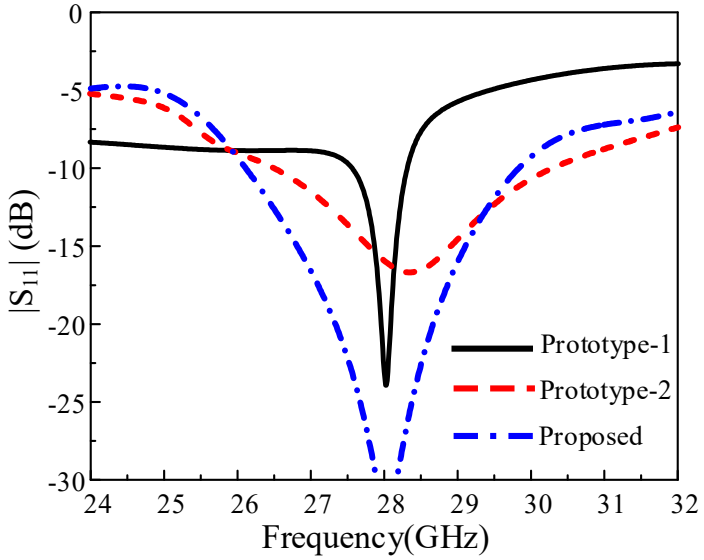

Figure 3. $|S_{11}|$ of the various antennas used in the design of the proposed antenna.

Thus, to further improve the bandwidth of the antenna and radiation characteristics, the symmetric T-shaped antenna designed in the first step was modified as an asymmetric T-shaped antenna, as depicted in Figure 2. The asymmetric structure changed the current distribution on the surface and resulted in increased current flowing through the large arm compared to the short arm of the T-shaped head, as depicted in Figure 4. This redistribution of current and unbalanced geometrical configuration resulted in more electromagnetic waves bending in a specific direction and, therefore, an end-fire radiation pattern, as depicted in Figure 5. Moreover, it was also observed that the impedance bandwidth of the modified T-shaped antenna increased from 650 MHz to 4300 MHz, with a range

of 26.9–31.1 GHz, and the gain improved from 3.96 GHz to 5.11 dB, as illustrated in Figures 3 and 5, respectively.

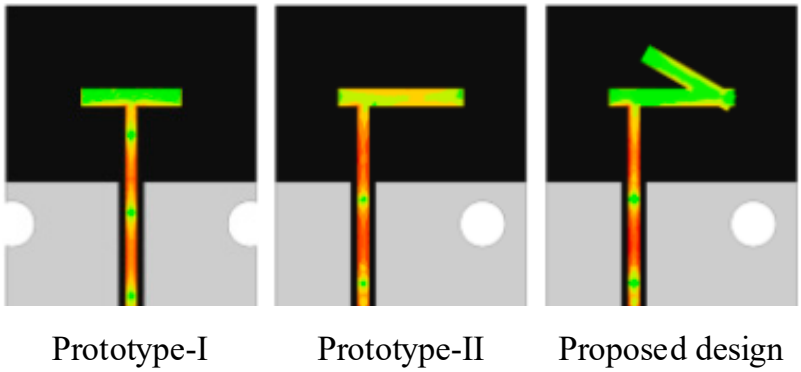

Figure 4. Surface charge distribution (at 28 GHz) of various steps in the antenna design.

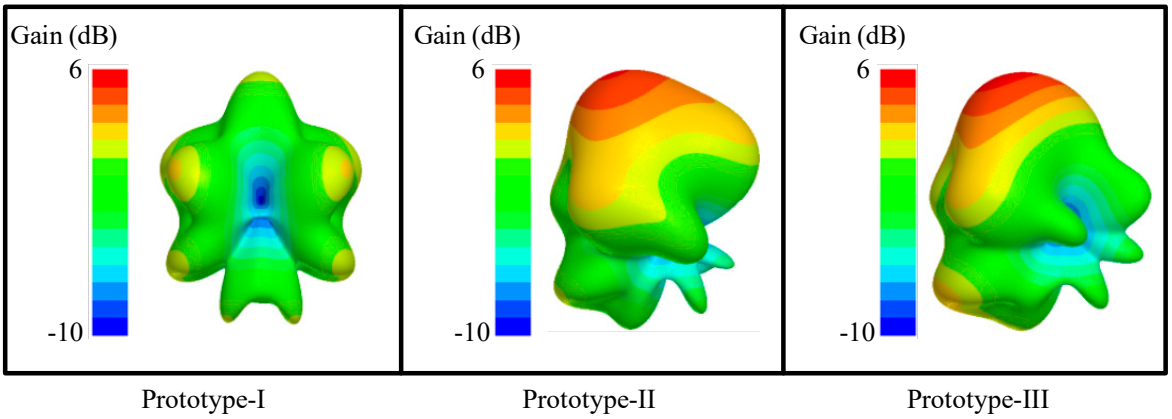

Figure 5. Radiation pattern of various steps in the design of proposed antenna.

In the final step, a single turn helix-inspired antenna was formed, as depicted in Figure 2. Helix antennas are well known for their end-fire radiation pattern if they satisfy the conditions for the axial mode of operation and their broadband operation. However, the conventional helix antenna requires a larger volume, therefore, planar helix antennas are becoming popular [31]. The equivalent models of an uncoiled single turn helix and a conventional helix are depicted in Figure 6. The planar configuration of the helix antenna uses the following parameters, as discussed in [32]: the diameter of the helix (D), the circumference of the helix (C = πD), the spacing between helix turns (x), the total length of the single turn ($L_T = \sqrt{C^2 + x^2}$), and the pitch angle ($\theta = \sin^{-1}\frac{x}{L_T}$). In most planar helix antennas, the top and bottom arms are connected by means of a via to form a single turn, however, the insertion of a via results in additional unwanted inductance which may affect antenna performance. Thus, to overcome the aforementioned challenge in the presented work, a via free single turn helix antenna was formed by placing two arms on the top side of the substrate. A helix antenna only radiates in the end-fire direction if it satisfies the following relation for operation in the axial mode: $\frac{3}{4} < C < \frac{4}{3}$ [32]. Therefore, the selected spacing between the helix arms is $x = \frac{\lambda}{4}$ and the relation between the circumference and the free space wavelength at the central frequency of 28 GHz was chosen to be $\frac{C}{\lambda} = 1$, to satisfy the relation for the end-fire radiation pattern. The optimized pitch angle was found to be 30°, which was selected after a detailed numerical analysis. The resultant antenna and its corresponding S-parameter results are depicted in Figures 2 and 3. The antenna exhibits broad impedance bandwidth of 3.8 GHz, ranging from 26 GHz to

29.8 GHz for $|S11| < -10$ dB, covering the globally allocated band spectrum of 28 GHz. The numerically calculated gain of the helix-inspired antenna was reported to be 5.92 dB with an end-fire radiation pattern, as depicted in Figure 5. It is important to note that in all three steps the dimension of the ground plane remains unchanged. The optimized parameters of the proposed antenna are as follows: A_Y = 15 mm; A_X = 10 mm; L_1 = 5 mm; L_2 = 3 mm; L_3 = 7 mm; W_1 = 3 mm; W_2 = 6 mm; P_1 = 5 mm; P_2 = 4 mm; d = 0.7 mm; f = 0.45 mm; θ = 30°.

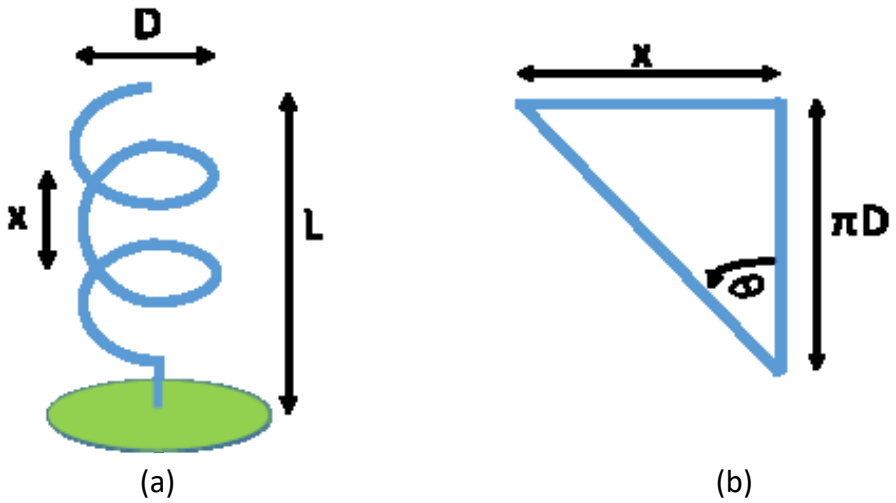

Figure 6. Demonstration of (**a**) conventional helix and (**b**) equivalent model of single turn planar helix.

2.3. Parametric Analysis

Changing the diameter of the helix eventually changes the circumference of the helix, which in turn changes the wavelength of the resonating antenna, because the previously selected relation for the end-fire radiation pattern was $\frac{C}{\lambda} = 1$. The change in wavelength (λ) shifts the frequency, and the radiation pattern is also affected, due to the relation $\frac{3}{4} < C < \frac{4}{3}$. Therefore, the diameter of the helix, which is equal to the length of the monopole, was not investigated. Other key parameters of the helix-inspired antenna were pitch angle, the total length of single helix turns, and spacing between helix turns. By changing the pitch angle, other parameters attain new values because they depend upon each other, therefore, the parametric analysis of the pitch angle is presented in this section.

By reducing the pitch angle (θ) from 30° to 15°, x corresponds to 1.1 mm and L_T corresponds to 11 mm. In this case, the antenna shows poor performance in terms of return loss, and the resonating frequency shifts to the higher side, whereas the targeted 28 GHz band was notched from the resonating region, as depicted in Figure 7. It can also be observed that, in this case, the gain of the antenna decreases from 5.92 dB to 3.89 dB and the back lobes become more prominent, as illustrated in Figure 8. In contrast, when the value of θ was increased from 30° to 45°, then x and L_T correspond to 2.43 mm and 11.27 mm, respectively. In this case, the resonating frequency of the antenna was slightly shifted toward the lower side, with the disadvantage of reduced bandwidth and poor impedance matching, as depicted in Figure 7. Moreover, it was also observed that the gain of the antenna also decreases from 5.92 dB to 5.05 dB, and the radiation pattern of the antenna is also distorted from purely end-fire to dual-beam, as depicted in Figure 8. Thus, it can be concluded from the aforementioned discussion that the presented antenna shows the best performance with optimized values of θ = 30°, x = 1.67 mm, L_T = 11.13 mm.

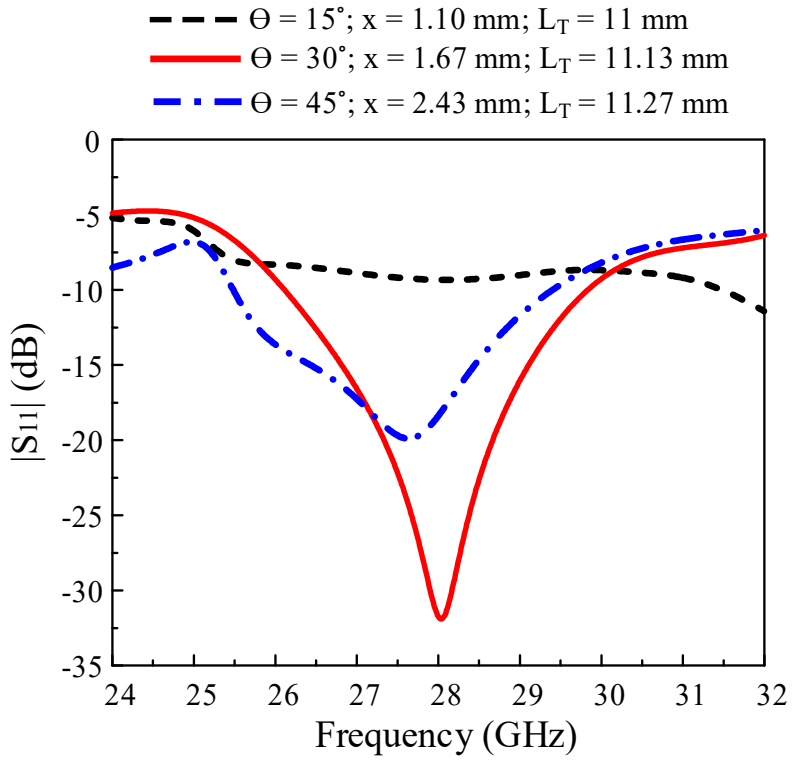

Figure 7. Return loss of antenna for various values of pitch angle (θ).

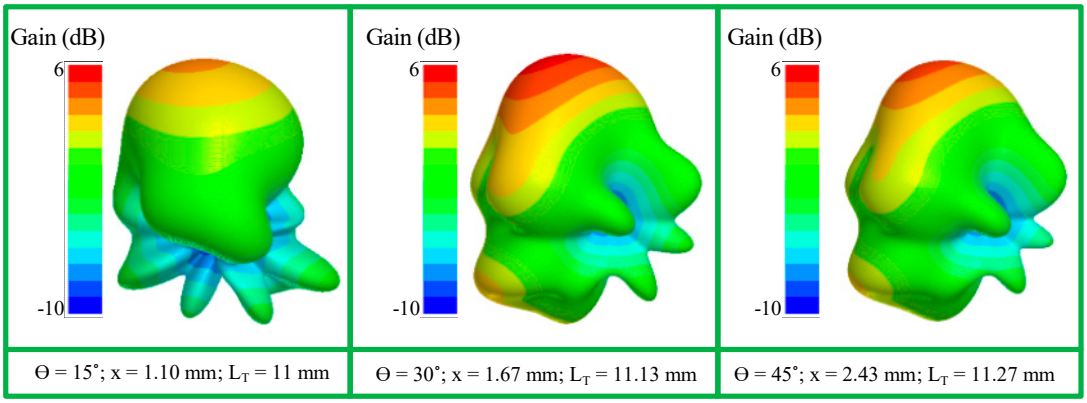

Figure 8. Radiation pattern and gain of the antenna for various values of pitch angle (θ).

3. Results and Discussion

3.1. Single Element

To verify the numerical findings, a prototype of the proposed antenna was fabricated and tested as shown in the inset of Figure 9. The standard chemical etching method was adopted to fabricate the antenna, and an end-launch connector by South West Corp. was used to excite the antenna. It is important to mention that the end-launch connector has been used to demonstrate the concept due its better performance and ease of use in 28 GHz mm-wave designs [33–35].

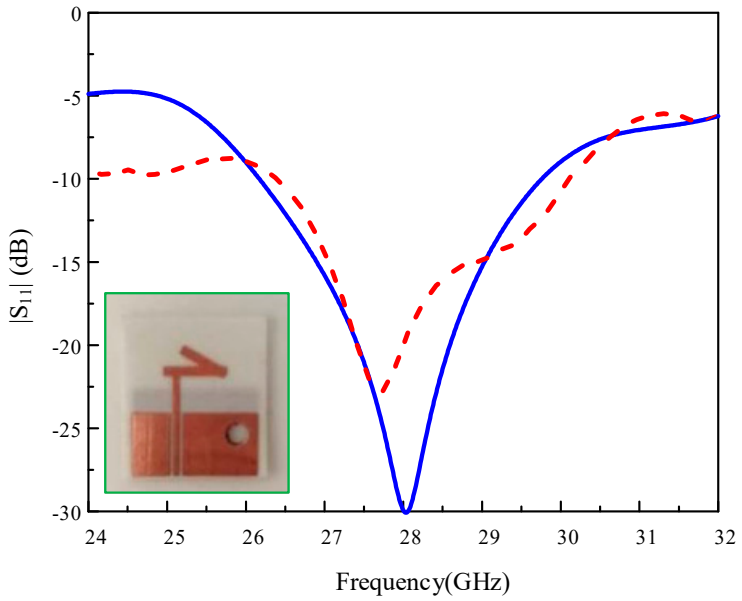

Figure 9. Simulated and measured return loss of the proposed antenna.

3.1.1. Return Loss

Figure 9 presents the comparison between the simulated and measured return loss of the proposed antenna. It can be seen that the antenna exhibits an impedance bandwidth of 3.8 GHz, ranging from 26 GHz to 29.8 GHz, and the measured impedance bandwidth was observed to be 3.89 GHz, ranging from 26.25 GHz to 30.14 GHz for $|S11| < -10$ dB. The small discrepancy between numerically calculated and tested results occurred due to imperfections in fabrication and the measurement setup.

3.1.2. Far-Field Results

Figure 10 presents the far-field results of the proposed antenna. Measurements were carried out using an anechoic chamber. It can be seen that antenna exhibits an end-fire radiation pattern in the principal E-plane ($\phi = 0°$), where the main lobe is pointed toward $\theta = -105°$. A similar pattern is also observed in the H-plane ($\phi = 90°$), where the main lobe is pointed toward $\theta = -135°$. A good agreement between simulated and measured radiation patterns was observed for both E- and H-planes. The antenna possesses a simulated and measured peak gain of < 5.83 dB in the operational bandwidth, and the numerically calculated and measured radiation efficiency of the antenna was also reported <85% in the achieved band, as depicted in Figure 10b.

3.2. MIMO Antenna

MIMO communication systems have gained considerable attention during the past decade due to the advantage of enhanced data throughput under the effects of signal interference, multiple paths, and signal fading. Consequently, to satisfy the basic requirements of the MIMO communication system, i.e., a MIMO antenna, the proposed antenna was further transformed into a MIMO antenna by placing two identical elements orthogonal to each other. The fabricated prototype of the MIMO antenna was used to test the various MIMO performance parameters, including scattering parameters (i.e., both reflection and transmission coefficients), envelope correlation coefficient (ECC), channel capacity loss (CCL), pattern diversity, diversity gain (DG), and mean effective gain (MEG).

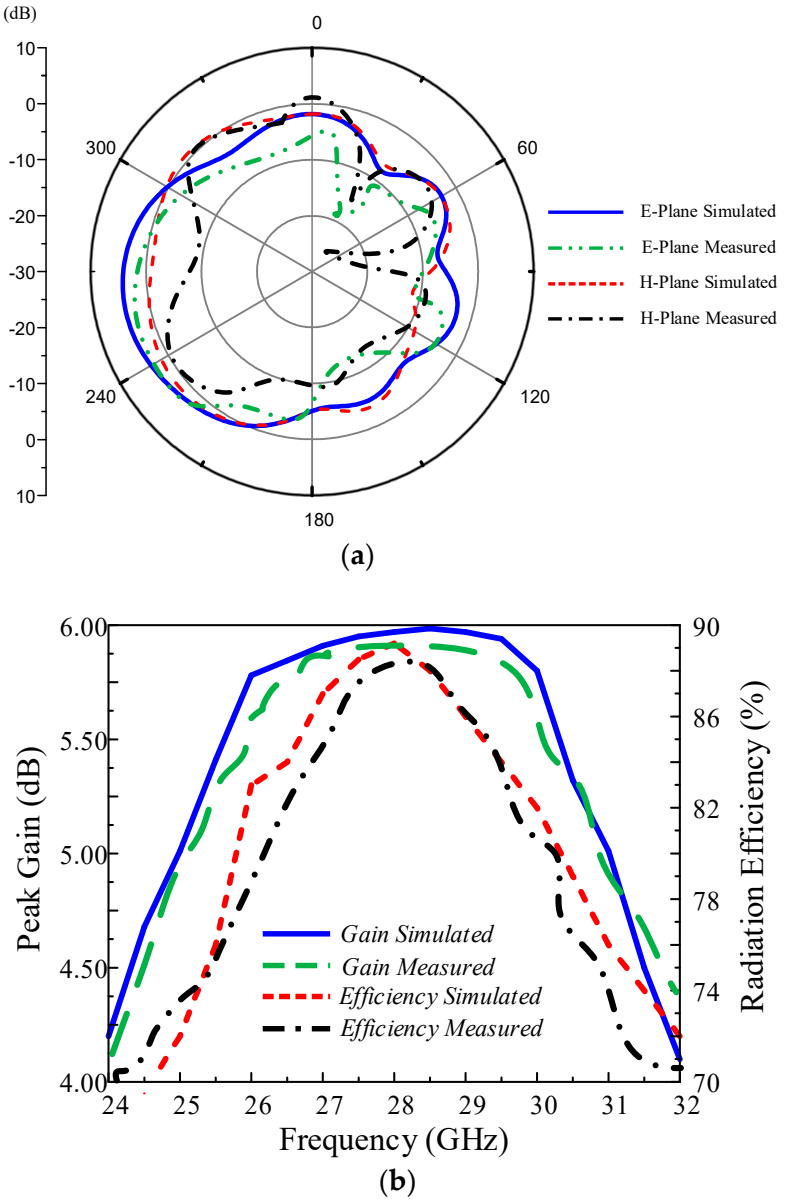

Figure 10. Comparison between simulated and measured (**a**) radiation pattern at 28 GHz, and (**b**) gain and radiation efficiency.

3.2.1. Scattering Parameters

A comparison between the simulated and measured value of reflection ($|S_{11}|$) and transmission coefficients ($|S_{12}|$) is presented in Figure 11. It can be observed that the simulated and measured reflection bandwidths are from 26–29.8 GHz and 26.25–30.14 GHz, respectively. The simulated value of $|S_{12}|$ was observed to be <−30 dB over the complete operational region, and the measured value of $|S_{12}|$ was observed to be less than −31 dB. Moreover, the minimum value of −57 dB was observed at the frequency of 27.61 GHz. The small discrepancy between numerically calculated and tested results occurred due to imperfections in fabrication and the measurement setup.

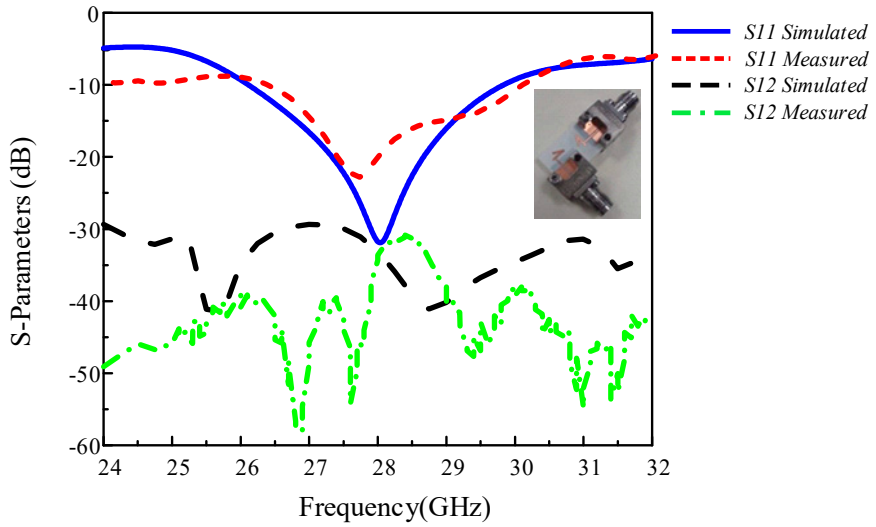

Figure 11. Simulated and measured scattering parameters of the multiple-input-multiple-output (MIMO) antenna.

3.2.2. Envelope Correlation Coefficient (ECC)

The envelope correlation coefficient (ECC) defines how one antenna is independent in its performance with respect to another antenna. Ideally, the value of ECC should be 0, however, for real cases, ECC < 0.5 is acceptable. ECC can be calculated using the following relation, provided in [36]:

$$\mathrm{ECC} = \frac{\left|S_{11}^{*}\, S_{12} + S_{21}^{*}\, S_{22}\right|^{2}}{\left(1 - |S_{11}|^{2} - |S_{21}|^{2}\right)\left(1 - |S_{22}|^{2} - |S_{12}|^{2}\right)} \tag{3}$$

For the presented antenna, the simulated value of ECC is <0.013, whereas the measured value was observed to be <0.005, as depicted in Figure 12a. The value of the proposed antenna is due to low mutual coupling and thus one element has less impact on the performance of the other element of the MIMO antenna.

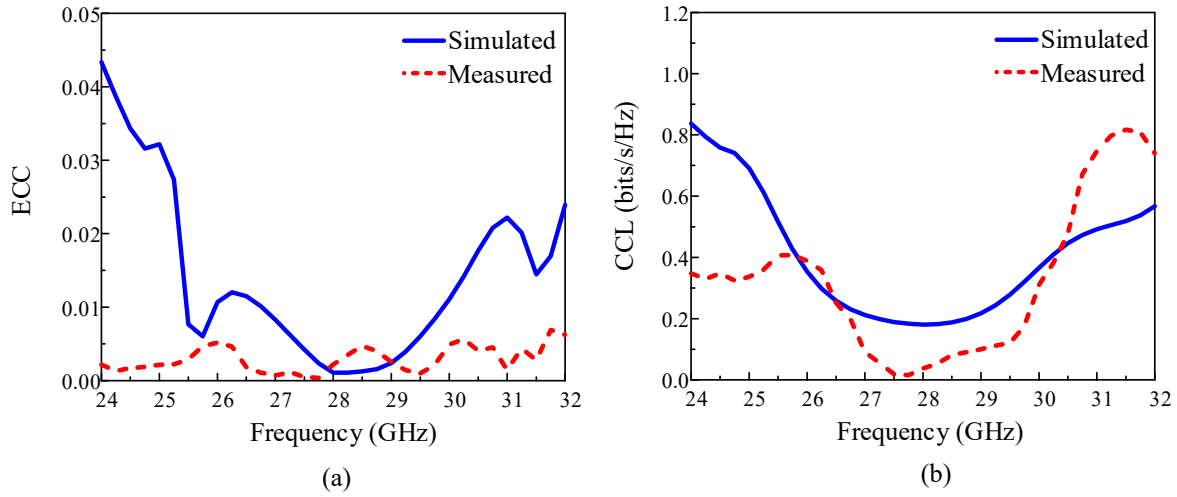

Figure 12. Simulated and measured: (**a**) envelope correlation coefficient (ECC) and (**b**) channel capacity loss (CCL).

3.2.3. Channel Capacity Loss (CCL)

Channel capacity loss (CCL) refers to the losses which may occur in the system due to correlation effects. The unit of CCL is bits/s/Hz and 0.5 is the maximum acceptable value for a system. CCL of any MIMO antenna can be calculated using the following relation [36]:

$$CCL = -log_2(1-|S_{ii}|^2-|S_{ij}|_2) \quad (4)$$

For the presented antenna, the value of $i = j = 1, 2$. Therefore, the simulated value of the MIMO antenna is <0.2 bits/s/Hz, whereas the measured value was observed to be <0.12 bits/s/Hz, as demonstrated in Figure 12b. Both simulated and measured values are less than the acceptable range of CCL, thus the presented MIMO antenna has a simple effect on the diversity performance of the system.

3.2.4. Pattern Diversity

Because the antenna radiates in the end-fire direction, the MIMO antenna elements were placed orthogonal to each other to achieve pattern diversity. Figure 13 illustrates the pattern diversity performance of the MIMO antenna when either port-1 or port-2 were excited. When port-1 is excited, the antenna shows a peak value of the radiation pattern located at θ = −105° in the E-plane, and the maximum beam was observed in the H-plane pointed toward θ = −115°. When port-2 is excited, the antenna exhibits an end-fire radiation pattern pointed toward θ = 115° in the principal E-plane, whereas for the principal H-plane, the antenna maximum beam was directed toward θ = −110°. Thus, the pattern of the proposed antenna can be switched from the +x-axis to the −y-axis depending upon the user requirements.

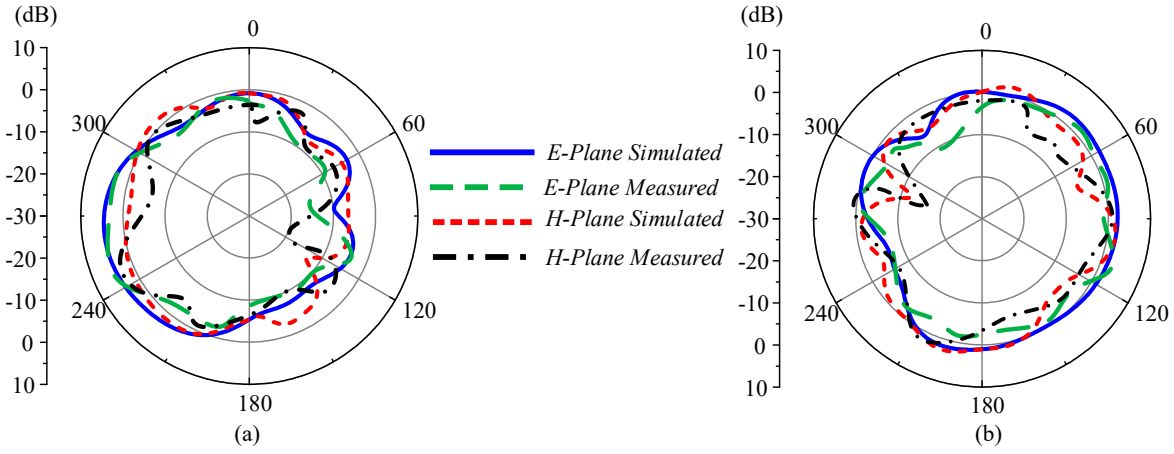

Figure 13. Simulated and measured radiation patterns for (**a**) port-1 and (**b**) port-2.

3.2.5. Diversity Gain (DG)

Diversity gain (DG) is one of the key parameters for any MIMO antenna system and is defined as the loss occurring in transmission power when the diversity scheme is performed. The DG can be calculated by using the ECC of the MIMO antenna by following relation [37]:

$$DG = 10\sqrt{1 - ECC^2} \quad (5)$$

The ideal case, in which ECC is 0, results in DG = 10 dB. Consequently, for the real case, the ECC should be very small so that DG must be approximately equal to 10 dB. For the presented case, the simulated results show that the antenna exhibits diversity gain of >9.998 dB, whereas the measured results depict DG >9.999 dB, as depicted in Figure 14a. Thus, the low value of ECC eventually results in a high value of DG, which makes the proposed antenna a strong candidate for diversity applications.

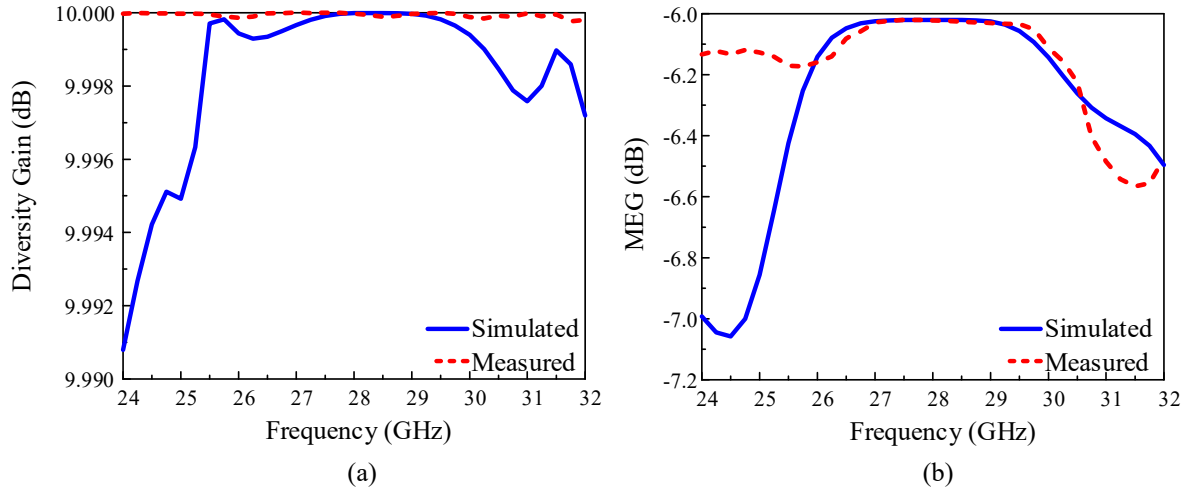

Figure 14. Simulated and measured (**a**) diversity gain and (**b**) mean effective gain.

3.2.6. Mean Effective Gain (MEG)

Another key parameter for diversity applications is mean effective gain (MEG) of the MIMO antenna, which is defined as the mean of received power by a system inside a fading environment. The value of MEG can be calculated using the following relation, given in [37]:

$$\text{MEG} = 0.5 \times \mu_{ir} = 0.5 \times \left[1 - \sum_{j=1}^{l} \left(|S_{ij}|\right)\right] \quad (6)$$

For the proposed MIMO antenna $l = 2$, $i = j = 1, 2$, where μ_{ir} represents the efficiency of the element of the MIMO antenna under observation. Practically, the acceptable value of MEG should be less than −3 dB. It can be observed that, for both simulation and measurement results, the MEG value is within the acceptable range, as depicted in Figure 14b. Thus, the good agreement between simulated and measured results of various performance parameters of the MIMO antenna validates the potential of the proposed work for MIMO and diversity applications.

3.3. Comparison with State-of-the-Art Works

The presented antenna is compared in Table 1 with the state-of-the-art mm-wave end-fire antennas to show the worth of this design. It can be noted that the presented antenna exhibits a compact size compared to [23–26], although the antenna presented in [22] has a compact size, but has limited bandwidth and low gain. Conversely, the gain values reported by [23–26] were higher than those of the current study, but they exhibit bigger dimensions, a via-based design [24–26], and less bandwidth [24,26]. Moreover, to provide a closer examination of MIMO performance, a comparison of the proposed MIMO antenna with other 28 GHz MIMO antennas is presented in Table 2. The proposed MIMO antenna exhibits very low mutual coupling, and low values of ECC and CCL, and a high value of DG was also observed. Therefore, it can be deduced from the aforementioned discussion that the presented end-fire antenna outperforms the related work due to its compact dimension, wide operational bandwidth, and moderate gain value, in addition to its via-free design, good MIMO antenna performance parameters, and pattern diversity for MIMO applications.

Table 1. Comparison of the proposed antenna with state-of-the-art end-fire antennas.

Refs.	Dimension ($\lambda_C \times \lambda_C$)	Fractional Bandwidth (%)	Peak Gain (dB)	Via Free Design
[22]	0.45 × 0.33	3.0	3.2	No
[23]	5.6 × 1.6	16.7	11.8	Yes
[24]	3.1 × 1.7	11.7	12.0	No
[25]	2.9 × 1.35	25.5	6.3	No
[26]	4.05 × 1.89	12.5	7.8	No
Proposed (Single element)	1.36 × 0.9	14.0	5.9	Yes

Table 2. Comparison of proposed MIMO antenna with related works for 28 GHz applications.

Refs.	Dimensions (mm × mm × mm)	No. of Ports	Mutual Coupling (dB)	ECC/CCL (bits/s/Hz)	DG (dB)/MEG (dB)	Pattern Diversity
[3]	20 × 20 × 7.608	4	<−25	<0.005/N.R.	N.R./N.R.	No
[12]	31.7 × 53 × 4	2	<−20	<0.120/N.R.	>9.40/N.R.	No
[13]	12.7 × 50.8 × 0.8	4	<−22	<0.150/N.R.	N.R./N.R.	No
[18]	30 × 35 × 0.76	4	<−20	<0.010/<0.40	>9.96/<−6.6	No
[36]	40 × 75 × 0.76	4	<−22	<0.015/<0.25	>9.83/<−6.6	No
[37]	20.4 × 20.4 × 0.5	4	<−30	<0.015/<0.19	>9.91/N.R.	No
Proposed	15 × 25 × 0.203	2	<−30	<0.005/<0.12	>9.95/<−6.0	Yes

4. Conclusions

In this paper, a planar helix-inspired wideband antenna for 28 GHz 5G applications was presented. The antenna geometry was extracted from a grounded-CPW fed T-shaped antenna by transforming it into an asymmetric antenna. Then, the concept of the planar helix antenna was utilized to improve the performance of the antenna. The via-free antenna offers a compact size of $1.36\lambda_C \times 0.9\lambda_C$ while exhibiting wideband measured impedance bandwidth of 3.89 GHz (26.25–30.14 GHz), with an end-fire radiation pattern having a maximum measured gain of 5.83 dB and maximum radiation efficiency of 88%. A single element was also utilized to design a MIMO antenna system, in which both elements were placed orthogonal to each other to achieve pattern diversity. The MIMO antenna showed parameter measurements of ECC < 0.005, CCL < 0.12 bits/s/Hz, and DG > 9.99 over the entire resonating bandwidth. The performance of the presented antenna was compared with state-of-the-art end-fire antennas and it could be observed that antenna outperforms related works due to its better performance.

Author Contributions: H.Z., W.A.A., W.A.E.A., N.H., S.M.A. and S.M., all authors equally contributed for developing methodology, performance analysis and drafting the manuscript. All authors have read and agreed to the published version of the manuscript.

Funding: This research received no external funding.

Conflicts of Interest: The authors declare no conflict of interest.

References

1. Andrews, J.G.; Buzzi, S.; Choi, W.; Hanly, S.V.; Lozano, A.; Soong, A.C.; Zhang, J.C. What Will 5G Be? *IEEE J. Sel. Areas Commun.* **2014**, *32*, 1065–1082. [CrossRef]
2. Asif, S.Z. *5G Mobile Communications: Concepts and Technologies*; CRC Press: Boca Raton, FL, USA, 2018.
3. Hussain, N.; Jeong, M.; Park, J.; Kim, N. A broadband circularly polarized fabry-perot resonant antenna using a single-layered PRS for 5G MIMO applications. *IEEE Access* **2019**, *7*, 42897–42907. [CrossRef]
4. Li, Y.; Yang, G. Dual-mode and triple-band 10-antenna handset array and its multiple-input multiple-output performance evaluation in 5G. *Int. J. RF Microw. Comput. Aided Eng.* **2019**, *29*, 21538. [CrossRef]
5. Inam, M.; Dahri, M.H.; Jamaluddin, M.H.; Seman, N.; Kamarudin, M.R.; Sulaiman, N.H. Design and characterization of millimeter wave planar reflectarray antenna for 5G communication systems. *Int. J. RF Microw. Comput. Aided Eng.* **2019**, *29*, 21804. [CrossRef]

6. Zaidi, A.; Awan, W.A.; Hussain, N.; Baghdad, A. A wide and tri-band flexible antennas with independently controllable notch bands for sub-6-GHz communication system. *Radioengineering* **2020**, *29*, 44–51. [CrossRef]
7. Hussain, N.; Jeong, M.J.; Abbas, A.; Kim, T.J.; Kim, N. A metasurface-based low-profile wideband circularly polarized patch antenna for 5G millimeter-wave systems. *IEEE Access* **2020**, *8*, 22127–22135. [CrossRef]
8. Zou, H.; Li, Y.; Sim, C.Y.D.; Yang, G. Design of 8 × 8 dual-band MIMO antenna array for 5G smartphone applications. *Int. J. RF Microw. Comput. Aided Eng.* **2018**, *28*, 21420. [CrossRef]
9. Pezhman, M.M.; Heidari, A.A.; Yazdi, A.G. Compact three-beam antenna based on SIW multi-aperture coupler for 5G applications. *AEU-Int. J. Electron. Commun.* **2020**, *123*, 153302. [CrossRef]
10. Sharma, M.; Gautam, A.K.; Agrawal, N.; Singh, N. Design of an antipodal balanced taper-fed broadband planar antenna for future 5G and remote sensing satellite link applications. *AEU-Int. J. Electron. Commun.* **2020**, *123*, 153292. [CrossRef]
11. Jeong, M.J.; Hussain, N.; Park, J.W.; Park, S.G.; Rhee, S.Y.; Kim, N. Millimeter-wave microstrip patch antenna using vertically coupled split ring metaplate for gain enhancement. *Microw. Opt. Technol. Lett.* **2019**, *61*, 2360–2365. [CrossRef]
12. Saad, A.A.R.; Mohamed, H.A. Printed millimeter-wave MIMO-based slot antenna arrays for 5G networks. *AEU-Int. J. Electron. Commun.* **2019**, *99*, 59–69. [CrossRef]
13. Jilani, S.F.; Alomainy, A. Millimetre-wave T-shaped MIMO antenna with defected ground structures for 5G cellular networks. *IET Microw. Antennas Propag.* **2018**, *12*, 672–677. [CrossRef]
14. Ullah, H.; Tahir, F.A. A wide-band rhombus monopole antenna array for millimeter wave applications. *Microw. Opt. Technol. Lett.* **2020**, *62*, 2111–2117.
15. Mneesy, T.S.; Hamad, R.K.; Zaki, A.I.; Ali, W.A.E. A novel high gain monopole antenna array for 60 GHz millimeter-wave communications. *Appl. Sci.* **2020**, *10*, 4546. [CrossRef]
16. Ali, W.; Das, S.; Medkour, H.; Soufian, L. Planar dual-band 27/39 GHz millimeter-wave MIMO antenna for 5G applications. *Microsyst. Technol.* **2020**, *27*, 283–292. [CrossRef]
17. Naqvi, S.I.; Naqvi, A.H.; Arshad, F.; Riaz, M.A.; Azam, M.A.; Khan, M.S.; Amin, Y.; Loo, J.; Tenhunen, H. An integrated antenna system for 4G and millimeter-wave 5G future handheld devices. *IEEE Access* **2019**, *7*, 116555–116566. [CrossRef]
18. Khalid, M.; Iffat Naqvi, S.; Hussain, N.; Rahman, M.; Mirjavadi, S.S.; Khan, M.J.; Amin, Y. 4-Port MIMO Antenna with defected ground structure for 5G millimeter wave applications. *Electronics* **2020**, *9*, 71. [CrossRef]
19. Zhang, J.; Zhao, K.; Wang, L.; Zhang, S.; Pedersen, G.F. Dual-Polarized Phased Array with End-Fire Radiation for 5G Handset Applications. *IEEE Trans. Antennas Propag.* **2020**, *68*, 3277–3282. [CrossRef]
20. Hong, W.; Baek, K.; Lee, Y.; Kim, Y.G. Design and analysis of a low-profile 28 GHz beam steering antenna solution for Future 5G cellular applications. In Proceedings of the 2014 IEEE MTT-S International Microwave Symposium (IMS2014), Tampa, FL, USA, 1–6 June 2014; pp. 1–4.
21. Ta, S.X.; Choo, H.; Park, I. Broadband Printed-Dipole Antenna and Its Arrays for 5G Applications. *IEEE Antennas Wirel. Propag. Lett.* **2017**, *16*, 2183–2186. [CrossRef]
22. Park, J.; Choi, D.; Hong, W. 28 GHz 5G dual-polarized end-fire antenna with electrically-small profile. In Proceedings of the 12th European Conference on Antennas and Propagation (EuCAP 2018), London, UK, 9–13 April 2018; pp. 1–4.
23. Guraliuc, A.R.; Chahat, N.; Leduc, C.; Zhadobov, M.; Sauleau, R. End-fire antenna for BAN at 60 GHz: Impact of bending, on-body performances, and study of an on to off-body scenario. *Electronics* **2014**, *3*, 221–233. [CrossRef]
24. Dadgarpour, A.; Zarghooni, B.; Virdee, B.S.; Denidni, T.A. Millimeter-wave high-gain SIW end-fire bow-tie antenna. *IEEE Trans. Antennas Propag.* **2015**, *63*, 2337–2342. [CrossRef]
25. Naqvi, A.H.; Park, J.H.; Baek, C.W.; Lim, S.J. V-band end-fire radiating planar micromachined helical antenna using through-glass silicon via (TGSV) technology. *IEEE Access* **2019**, *7*, 87907–87915. [CrossRef]
26. Naqvi, A.H.; Park, J.H.; Baek, C.W.; Lim, S.J. Via-monopole based quasi yagi-uda antenna for W-band applications using through glass silicon via (TGSV) technology. *IEEE Access* **2020**, *8*, 9513–9519. [CrossRef]
27. Chen, Z.; Shen, Z. Planar Helical Antenna of Circular Polarization. *IEEE Trans. Antennas Propag.* **2015**, *63*, 4315–4323. [CrossRef]
28. Syrytsin, I.; Zhang, S.; Pedersen, G.F. Circularly polarized planar helix phased antenna array for 5G mobile terminals. In Proceedings of the 2017 International Conference on Electromagnetics in Advanced Applications (ICEAA), Verona, Italy, 11–15 September 2017; pp. 1105–1108.
29. 'Rogers Corporation'. Available online: www.rogerscorp.com (accessed on 29 June 2020).
30. Awan, W.A.; Hussain, N.; Le, T.R. Ultra-thin flexible fractal antenna for 2.45 GHz application with wideband harmonic rejection. *AEU-Int. J. Electron. Commun.* **2019**, *110*, 152851. [CrossRef]
31. Balanis, C.A. *Antenna Theory: Analysis and Design*; John Wiley & Sons: Hoboken, NJ, USA, 2009.
32. Stutzman, W.L.; Thiele, G.A. *Antenna Theory and Design*; Wiley: Hoboken, NJ, USA, 2012.
33. Alhalabi, R.A.; Rebeiz, G.M. High-Efficiency Angled-Dipole Antennas for Millimeter-Wave Phased Array Applications. *IEEE Trans. Antennas Propag.* **2008**, *56*, 3136–3142. [CrossRef]
34. Koul, S.K.; Karthikeya, G.S.; Poddar, A.K.; Rohde, U.L. Compact Antenna Designs for Future mmWave 5G Smart Phones. *Microw. J.* **2020**, *63*, 22–40.
35. Karthikeya, G.S.; Abegaonkar, M.P.; Koul, S.K. CPW Fed Wideband Corner Bent Antenna for 5G Mobile Terminals. *IEEE Access* **2019**, *7*, 10967–10975. [CrossRef]

36. Naqvi, S.I.; Hussain, N.; Iqbal, A.; Rahman, M.; Forsat, M.; Mirjavadi, S.S.; Amin, Y. Integrated LTE and millimeter-wave 5G MIMO antenna system for 4G/5G wireless terminals. *Sensors* **2020**, *20*, 3926. [CrossRef]
37. Hussain, N.; Jeong, M.J.; Abbas, A.; Kim, N. Metasurface-based single-layer wideband circularly polarized MIMO antenna for 5G millimeter-wave systems. *IEEE Access* **2020**, *8*, 130293–130304. [CrossRef]